Onset of collectivity for argon isotopes close to $N = 32$

B. D. Linh,[1,2] A. Corsi,[3] A. Gillibert,[3] A. Obertelli,[3,4,5] P. Doornenbal,[4] C. Barbieri,[6,7] T. Duguet,[3,8] M. Gómez-Ramos,[9] J. D. Holt,[10,11] B. S. Hu,[10] T. Miyagi,[5,12,13] A. M. Moro,[9,14] P. Navrátil,[10] K. Ogata,[15,16] S. Péru,[17,18] N. T. T. Phuc,[19,20] N. Shimizu,[21,22] V. Somà,[3] Y. Utsuno,[22,23] N. L. Achouri,[24] H. Baba,[4] F. Browne,[4] D. Calvet,[3] F. Château,[3] S. Chen,[4,25,26] N. Chiga,[4] M. L. Cortés,[4] A. Delbart,[3] J.-M. Gheller,[3] A. Giganon,[3] C. Hilaire,[3] T. Isobe,[4] T. Kobayashi,[27] Y. Kubota,[4,22] V. Lapoux,[3] H. N. Liu,[3,5,8] T. Motobayashi,[4] I. Murray,[4,29] H. Otsu,[4] V. Panin,[4] N. Paul,[3,30] W. Rodriguez,[4,31,32] H. Sakurai,[4,33] M. Sasano,[4] D. Steppenbeck,[4] L. Stuhl,[22,34,35] Y. L. Sun,[3,5] Y. Togano,[36] T. Uesaka,[4] K. Wimmer,[4,33] K. Yoneda,[4] O. Aktas,[28] T. Aumann,[5,37] L. X. Chung,[2] F. Flavigny,[24,29] S. Franchoo,[29] I. Gašparić,[4,5,38] R. B. Gerst,[39] J. Gibelin,[24] K. I. Hahn,[40,35] N. T. Khai,[1] D. Kim,[40,4,35] T. Koiwai,[33] Y. Kondo,[41] P. Koseoglou,[5,37,42] J. Lee,[25] C. Lehr,[5] T. Lokotko,[25] M. MacCormick,[29] K. Moschner,[39] T. Nakamura,[41] S. Y. Park,[40,35] D. Rossi,[5] E. Sahin,[43] D. Sohler,[34] P.-A. Söderström,[5,44] S. Takeuchi,[41] H. Törnqvist,[5,37] V. Vaquero,[45] V. Wagner,[5] S. T. Wang,[46] V. Werner,[5,42] X. Xu,[25] Y. Yamada,[41] D. Yan,[46] Z. Yang,[4] M. Yasuda,[41] and L. Zanetti[5]

[1]*Vietnam Agency for Radiation and Nuclear Safety, 113 Tran Duy Hung, Cau Giay, Hanoi 100000, Vietnam*
[2]*Institute for Nuclear Science & Technology, VINATOM, 179 Hoang Quoc Viet, Cau Giay, Hanoi, Vietnam*
[3]*Université Paris-Saclay, IRFU, CEA, F-91191 Gif-sur-Yvette, France*
[4]*RIKEN Nishina Center, 2-1 Hirosawa, Wako, Saitama 351-0198, Japan*
[5]*Institut für Kernphysik, Technische Universität Darmstadt, 64289 Darmstadt, Germany*
[6]*Dipartimento di Fisica "Aldo Pontremoli", Universita degli Studi di Milano, Via Celoria 16, I-20133 Milano, Italy*
[7]*INFN, Sezione di Milano, Via Celoria 16, I-20133 Milano, Italy*
[8]*KU Leuven, Instituut voor Kern- en Stralingsfysica, B-3001 Leuven, Belgium*
[9]*Departamento de Fisica Atomica Molecular y Nuclear, Facultad de Fisica, Universidad de Sevilla, Apartado 1065, E-41080 Sevilla, Spain*
[10]*TRIUMF, 4004 Wesbrook Mall, Vancouver, British Columbia V6T 2A3, Canada*
[11]*Department of Physics, McGill University, 3600 Rue University, Montréal, Quebec H3A 2T8, Canada*
[12]*ExtreMe Matter Institute EMMI, GSI Helmholtzzentrum für Schwerionenforschung GmbH, 64291 Darmstadt, Germany*
[13]*Max-Planck-Institut für Kernphysik, Saupfercheckweg 1, 69117 Heidelberg, Germany*
[14]*Instituto Interuniversitario Carlos I de Fisica Teorica y Computacional (iC1), Apdo. 1065, E-41080 Sevilla, Spain*
[15]*Department of Physics, Kyushu University, Fukuoka 819-0395, Japan*
[16]*Research Center for Nuclear Physics (RCNP), Osaka University, Ibaraki 567-0047, Japan*
[17]*CEA, DAM, DIF, F-91297 Arpajon, France*
[18]*Université Paris-Saclay, CEA, LMCE, 91680 Bruyères-le-Châtel, France*
[19]*Department of Nuclear Physics, Faculty of Physics and Engineering Physics, University of Science, Ho Chi Minh City 700000, Vietnam*
[20]*Vietnam National University, Ho Chi Minh City 700000, Vietnam*
[21]*Center for Computational Sciences, University of Tsukuba, 1-1-1 Tenno-dai, Tsukuba 305-8577, Japan*
[22]*Center for Nuclear Study, University of Tokyo, RIKEN campus, Wako, Saitama 351-0198, Japan*
[23]*Japan Atomic Energy Agency, Tokai, Ibaraki 319-1195, Japan*
[24]*LPC Caen, Normandié Universite, ENSICAEN, UNICAEN, CNRS/IN2P3, F-14000 Caen, France*
[25]*Department of Physics, The University of Hong Kong, Pokfulam 999077, Hong Kong*
[26]*State Key Laboratory of Nuclear Physics and Technology, Peking University, Beijing 100871, China*
[27]*Department of Physics, Tohoku University, Sendai 980-8578, Japan*
[28]*Department of Physics, Royal Institute of Technology, SE-10691 Stockholm, Sweden*
[29]*Université Paris-Saclay, CNRS/IN2P3, IJCLab, Orsay, France*
[30]*Laboratoire Kastler Brossel, Sorbonne Université, CNRS, ENS, PSL Research University, Collège de France, Case 74, 4 Place Jussieu, F-75005 Paris, France*
[31]*Departamento de Física, Pontificia Universidad Javeriana, Bogotá, Colombia*
[32]*Departamento de Fisica, Facultad de Ciencias, Universidad Nacional de Colombia, Sede Bogotá, Bogotá 111321, Colombia*
[33]*Department of Physics, University of Tokyo, 7-3-1 Hongo, Bunkyo, Tokyo 113-0033, Japan*
[34]*Institute for Nuclear Research, Atomki, P.O. Box 51, Debrecen H-4001, Hungary*
[35]*Institute for Basic Science, Daejeon 34126, Korea*
[36]*Department of Physics, Rikkyo University, 3-34-1 Nishi-Ikebukuro, Toshima, Tokyo 172-8501, Japan*
[37]*GSI Helmholtzzentrum fur Schwerionenforschung GmbH, Planckstr. 1, 64291 Darmstadt, Germany*
[38]*Ruđer Bošković Institute, Bijenička Cesta 54, 10000 Zagreb, Croatia*
[39]*Institut für Kernphysik, Universität zu Köln, D-50937 Koln, Germany*
[40]*Ewha Womans University, Seoul 03760, Korea*
[41]*Department of Physics, Tokyo Institute of Technology, 2-12-1 O-Okayama, Meguro, Tokyo 152-8551, Japan*

[42]*Helmholtz Forschungsakademie Hessen für FAIR (HFHF), GSI Helmholtzzentrum für Schwerionenforschung, Campus Darmstadt, 64289 Darmstadt, Germany*
[43]*Department of Physics, University of Oslo, N-0316 Oslo, Norway*
[44]*Extreme Light Infrastructure–Nuclear Physics (ELI-NP), Horia Hulubei National Institute for Physics and Nuclear Engineering (IFIN-HH), Str. Reactorului 30, Bucharest-Măgurele 077125, Romania*
[45]*Instituto de Estructura de la Materia, CSIC, E-28006 Madrid, Spain*
[46]*Institute of Modern Physics, Chinese Academy of Sciences, Lanzhou 730000, China*

(Received 28 June 2023; accepted 7 December 2023; published 19 March 2024)

The shell closure at $N = 32$ has been investigated by a first spectroscopy of the $N = 31$ nucleus ^{49}Ar at the Radioactive Isotope Beam Factory. Using the ^{50}Ar(p, pn) reaction channel in inverse kinematics, ^{50}Ar projectiles at 217 MeV/nucleon impinged on a 150 mm long liquid hydrogen target, part of the MINOS device. Prompt deexcitation γ rays were measured with the NaI(Tl) array DALI2$^+$. Reaction products were analyzed with the SAMURAI spectrometer, which allowed the measurement of the momentum distributions and angular momentum transfer. Data were compared to state-of-the-art theoretical predictions, including shell-model, energy-density functional, and *ab initio* calculations. An onset of collectivity is suggested besides the spherical configuration typical of a closed shell nucleus, such as for ^{52}Ca.

DOI: 10.1103/PhysRevC.109.034312

I. INTRODUCTION

The neutron number $N = 28$ is considered a magic number corresponding, in the standard shell-model picture, to a filled neutron $\nu 0f_{7/2}$ orbital and a well-defined energy gap. For stable nuclei, the main evidence of this shell closure is given by ^{48}Ca, combining observations from mass measurements, γ-ray spectroscopy, or transfer measurements [1]. However, shell closures evolve across the nuclear chart as a result of the delicate balance between the different correlations at play among the nucleons. For instance, when more proton-deficient $N = 28$ isotones are considered, an onset of quadrupole deformation is observed for nuclei such as ^{42}Si [2–4] or ^{40}Mg [5]. In contrast, $N = 32$ and 34 have been proposed to be new magic numbers [6], not observed for stable nuclei, corresponding to filled $\nu 1p_{3/2}$ and $\nu 1p_{1/2}$ orbitals, respectively.

Mass excesses for neutron-rich nuclei have been determined for Ca isotopes [7–9] up to ^{57}Ca. The characteristic behavior of the two-neutron separation energy S_{2n} at a major shell closure—relatively flat below and with a sharp decrease over two neutron units beyond–is clearly observed, not only at $N = 28$ but also at $N = 32$ for ^{52}Ca. This closure effect, shown by the global observable S_{2n}, has been confirmed by the measurements of the energy $E(2_1^+)$ of the first 2^+ state and the reduced transition probabilities $B(E2; 0_1^+ \rightarrow 2_1^+)$. A high value of $E(2_1^+)$, compared to the neighboring isotopes, was found for ^{48}Ca and ^{52}Ca [10,11]. This was further confirmed by the low values of $E(2_1^+)$ recently measured in ^{56,58}Ca [12]. A small $B(E2; 0_1^+ \rightarrow 2_1^+)$ value was found for ^{48}Ca [13,14], but is still missing for ^{52}Ca. Unexpectedly for a closed-shell nucleus, the large increase of the ^{52}Ca charge radius [15], compared to ^{48}Ca, is now attributed to a larger radius of the $\nu 1p_{3/2}$ orbital and isovector polarizability [16,17]. Additional converging information is provided by the analyses of neutron transfer reactions [18,19]. For ^{47}Ca, the $7/2_1^-$ ground state (gs) has a large spectroscopic factor C^2S, close to the $2j + 1$ limit compatible with a neutron hole state in the $\nu 0f_{7/2}$ orbital in ^{48}Ca. At the same time, small C^2S values were found for the $3/2^-$ states, consistent with little occupancy of the $\nu 1p_{3/2}$ orbital. Such information was still missing for ^{52}Ca until a recent analysis of the ^{52}Ca(p, pn) knockout [16].

These experimental results are strong enough to establish the concept of a shell closure for ^{48}Ca at $N = 28$, and arguably for ^{52}Ca at $N = 32$. However, such properties may not be as robust for light nuclei as they are for heavier nuclei where, for instance, $N = 82$ or 126 magic gaps are well established over a large range of atomic number Z. For isotopic series with $Z > 20$, a similar behavior, although weakening with increasing Z, has been observed for both $N = 28$ and $N = 32$ in titanium and chromium nuclei [20–22], with higher $E(2_1^+)$ and smaller $B(E2; 0_1^+ \rightarrow 2_1^+)$ values.

The isotopic distributions with $Z < 20$, such as the argon distribution, are less documented since they correspond to more neutron-rich nuclei. Mass measurements have extended the S_{2n} evolution to neutron-rich argon isotopes and are consistent with a shell closure at $N = 28$ [23,24]. A low $B(E2; 0_1^+ \rightarrow 2_1^+)$ value was also found for ^{46}Ar [13,25]. This value increases for ^{48}Ar [26] but is missing for more neutron-rich isotopes. High $E(2_1^+)$ values have been determined by in-beam γ-ray spectroscopy for ^{46}Ar [13] and ^{52}Ar [27], while $E(2_1^+)$ for ^{50}Ar [28,29] is comparatively reduced. However, the link between $E(2_1^+)$ and a shell closure effect may be discussed. In shell-model calculations performed with the SDPF-MU interaction [28], the 2_1^+ state for ^{52}Ca is understood as a neutron excitation $\nu 1p_{3/2} \rightarrow \nu 1p_{1/2}$ from a ground state dominated by a $(\nu 1p_{3/2})^4$ configuration (about 90%). Therefore, in this case, the large value of $E(2_1^+)$ is representative of the $N = 32$ energy gap. When removing two protons, the same calculation predicts for ^{50}Ar mixed configurations for the 0_1^+, 2_1^+, and 4_1^+ states, such that $E(2_1^+)$ is not so cleanly connected to the monopole energy gap. Furthermore, the analysis of the neutron pickup at $N = 28$

in the ^{46}Ar$(d, p)^{47}$Ar reaction suggests a partial occupation of the $\nu 0f_{7/2}$ orbital, while the spectroscopic factors of the $3/2^-$ states are consistent with a substantial occupancy of the $\nu 1p_{3/2}$ orbital [30]. Going further with the quadrupolar degree of freedom, theoretical calculations such as energy-density functional calculations feature shapes away from spherical [31,32] with competition between oblate and prolate minima, when protons are removed from Ca isotopes. This results, for example, in a weak oblate minimum predicted for the ground state of ^{46}Ar, but a dominant one for ^{42}Si, with a low $E(2_1^+)$ value measured for the latter [2–4]. The potential energy surfaces obtained for the $N = 32$ isotones ^{50}Ar, ^{48}S, and ^{46}Si in mean-field calculations with the Gogny effective interaction [33–35] are consistent with nuclei being rather soft against quadrupole deformation.

To get a better insight into the robustness of the subshell closure at $N = 32$, the one-neutron knockout reaction ^{50}Ar$(p, pn)^{49}$Ar has been used to provide information on hole states from the ^{50}Ar core. The aim is to determine the excitation energy and cross sections of the low-lying states in ^{49}Ar. Experimental data are compared to state-of-the-art theoretical predictions, including shell-model, energy-density functional, and *ab initio* calculations. In particular, the shell-model calculations also serve as a guideline for the experimental analysis.

This article is structured as follows. The experimental setup is described in Sec. II. The methods used for data analysis are developed in Sec. III, including the determination of momentum distributions and cross sections. In the same experiment, a similar analysis was performed on isotopes ^{47,49}Cl, which was extensively described in Ref. [36]. Therefore, here only the main features are recalled. A presentation of the experimental results for ^{49}Ar concludes Sec. III. Finally, an extensive discussion of the experimental findings and the theoretical calculations is the subject of Sec. IV.

II. EXPERIMENTAL SETUP

The experiment was performed at the Radioactive Isotope Beam Factory (RIBF), operated jointly by the RIKEN Nishina Center and the Center for Nuclear Study of the University of Tokyo. A ^{70}Zn beam was accelerated up to 345 MeV/nucleon for the production of a mixed secondary beam, including the ^{50}Ar beam, selected with the help of the BigRIPS separator [37] and identified with the magnetic rigidity $B\rho$, energy loss ΔE, and time of flight (TOF) measurements [38]. Within the MINOS setup [39], a 151(1) mm thick liquid hydrogen target was used to compensate for the low-intensity beams.

The incident energy at the entrance (exit) of the secondary target was ≈ 247 (≈ 184) MeV/nucleon, with an intensity of 2.9 particles/s for ^{50}Ar. The scattered ions were analyzed with the SAMURAI large acceptance spectrometer [40] behind the secondary target and identified by the mass-over-charge ratio A/Q and the atomic number Z. The unambiguous separation of the different projectiles and residues is shown in Fig. 1. Prompt γ rays emitted at the MINOS target were detected with the DALI2$^+$ array [41], composed of 226 NaI(Tl) detectors in a compact geometry. The target was surrounded by the cylindrical time-projection chamber of the MINOS setup [39], which was used for the determination of the reaction vertex and the Doppler-shift correction. The energy calibration of the DALI2$^+$ array and the procedure for Doppler-shift correction due to in-flight emission are given in Ref. [36].

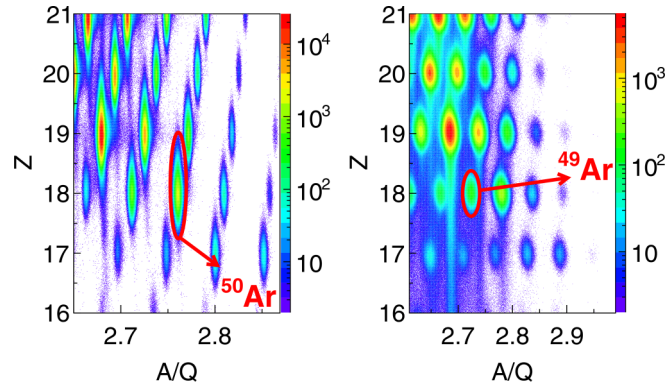

FIG. 1. Particle identification with the mass over charge ratio A/Q and atomic number Z. Left: beam particle identification at BigRIPS before the target. Right: residue particle identification downstream the secondary target from the large acceptance SAMURAI spectrometer. ^{50}Ar and ^{49}Ar in front and behind the MINOS secondary target are shown by the red ellipses.

III. SPECTROSCOPY OF ^{49}Ar

Different reaction channels have been used to study the bound states in ^{49}Ar below the one-neutron separation energy $S_n = 2780\,(400)$ keV [42]: (*i*) ^{50}Ar(p, pn), which is expected to populate single particle states by one-neutron knockout from the ^{50}Ar core; (*ii*) ^{51}K$(p, 2pn)$ with a more complex reaction mechanism possibly populating states at higher spin and higher excitation energy; (*iii*) inelastic scattering ^{49}Ar(p, p'), which favors the excitation of collective states from the ground state. The corresponding Doppler-corrected energy spectra are shown in Figs. 2(a) and 2(b) after subtraction of a low-energy background component. This subtraction, explained in Ref. [36], was also applied here since a low-energy transition was observed in ^{49}Ar at 198 keV: The low-energy bremsstrahlung component from the ^{49}Ar(p, p) scattering is normalized and subtracted in the spectra, except for the same channel in Fig. 2(c). Then, the single spectra were reproduced by a combination of response functions for transitions and a two-component exponential background with fitted amplitudes.

A. ^{50}Ar$(p, pn)^{49}$Ar

In a shell-model picture, the one-neutron knockout reaction is expected to populate states in ^{49}Ar, which have a sizable overlap with the neutron-hole configurations $(\nu 1p_{3/2})^{-1}$ and $(\nu 0f_{7/2})^{-1}$, assuming these orbitals to be filled in the $N = 32$ isotope ^{50}Ar. For a closed-shell nucleus, the $\nu 1p_{1/2}$ orbital should be nearly empty, resulting in a weak population of $1/2^-$ states in this direct reaction.

The one-neutron knockout spectrum in Fig. 2(a) displays an intense peak at 198 keV and a broad structure between 900 and 1600 keV on top of the background. There is no strong evidence for another transition at higher energy.

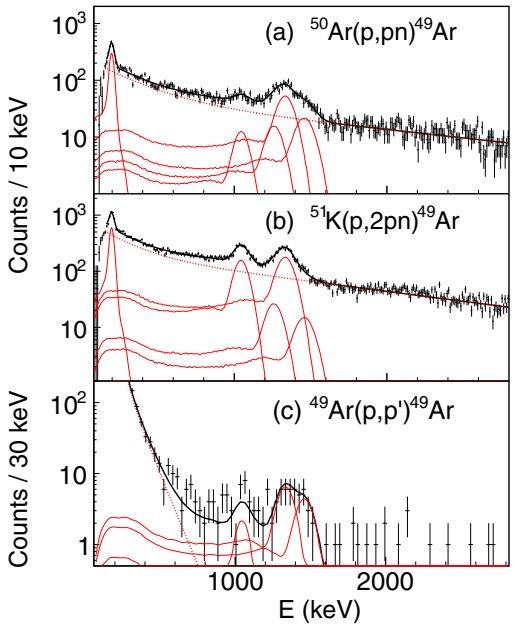

FIG. 2. Doppler-corrected γ-ray spectra of ^{49}Ar obtained from (a) one-neutron knockout ^{50}Ar(p, pn), (b) the more complex ^{51}K$(p, 2pn)$ reaction, and (c) inelastic scattering ^{49}Ar(p, p'). Spectra in (a) and (b) are obtained after subtraction of a low-energy bremsstrahlung component (see text). Experimental data (points) are fitted by a combination (black line) of five simulated DALI2$^+$ response functions (red continuous lines) and a two-component exponential background (red dashed line).

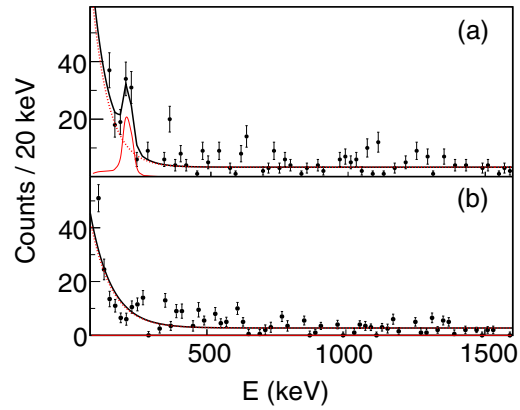

FIG. 3. Doppler-corrected γ-ray spectra of ^{49}Ar obtained from the one-neutron knockout ^{50}Ar(p, pn) (a) gated by the [1180,1320] range in Fig. 2(a), which maximizes the ratio of the response function corresponding to the 1266 keV transition over other transitions; (b) gated by the energy ranges just below and above, which maximizes the background due to other transitions.

The broad structure is reproduced mainly by three response functions corresponding to transitions at 1050, 1340, and 1466 keV.

γ-γ correlations were also examined with gates corresponding to the main transitions observed in the singles spectrum. No clear coincidence was observed in this first step. Then, a different procedure was used to determine a possible coincidence with the 198 keV transition due to the complex underlying Compton background. A moving gate was applied over the whole energy spectrum while searching for the 198 keV transition, and a significant coincidence with a confidence level of 5.5σ was found for the energy gate [1180,1320], keV as shown in Fig. 3(a). Due to fluctuations, no other transition could be significantly identified. No coincidence was found for gates at higher energies, dominated by the 1340 and 1466 keV transitions. Another spectrum is shown in Fig. 3(b) corresponding to the gates just below and above the [1180,1320] gate.

This is an indication of a possible coincidence between the transitions at 188 and 1266 keV, the latter being not clearly visible in the singles spectrum due to the overwhelming 1340 keV transition nearby. The summed energy of the coincidence is 1464 keV, consistent with the observed transition at 1466(21) keV. So it was included for the fits of the singles spectra of Fig. 2, even though its weight was dominated by the 1340 keV transition. Additionally, this 1266 keV transition was useful for reproducing the left side of the wide bump around 1300 keV.

The overlap of the Compton spectra included in the different response functions was sufficient to reproduce correctly the energy range between 200 and 900 keV without evidence of another strong transition.

Finally, the simplest reproduction of the histogram shown in Fig. 2(a) was obtained by a combination of response functions at 198(3), 1050(29), 1266(41), 1340(14), and 1466(21) keV, on top of a two-component exponential background.

The inelastic scattering ^{50}Ar(p, p') can populate collective states in ^{50}Ar above the one-neutron separation energy S_n = 4210 keV, which will decay and populate low lying states in ^{49}Ar. In the previous analysis, this contribution could not be distinguished from the direct one-neutron removal reaction channel, except for the neutron emitted at a very forward angle and detected with the NEULAND demonstrator [43] and the NEBULA array [44]. Similar analyses were already performed in [16,45] and the contribution was subtracted from the cross sections below.

B. Other reaction channels

A similar analysis was performed for the ^{51}K$(p, 2pn)$ ^{49}Ar channel in Fig. 2(b), using the response functions with the same centroid energies obtained for the ^{50}Ar(p, pn) ^{49}Ar reaction. They were sufficient to reproduce the experimental spectrum, with no evidence of another strong transition.

Compared to the intensity of the 1340 keV transition, one observes an intensity reduction of the 1466 keV transition and a strong intensity enhancement of the 1050 keV transition. This enhancement is consistent with the decay of a state which would be less populated in the direct neutron knockout, due to a small overlap with a neutron-hole configuration, than in a more complex reaction channel favoring a population of higher spin or higher-lying states. The intensity ratios I_i/I_{1050} are shown in Table I. The four other transitions are clearly enhanced in the one-neutron knockout. There was no evidence of a transition in coincidence with the 1050 keV transition.

TABLE I. Transitions observed in Fig. 2 for the two different reaction channels ^{50}Ar$(p, pn)^{49}$Ar and ^{51}K$(p, 2pn)^{49}$Ar: excitation energy E^*, detection-efficiency corrected intensity I_i, and intensity ratios normalized to the 1050 and 1340 keV transitions.

E^*	^{50}Ar$(p, pn)^{49}$Ar			^{51}K$(p, 2pn)^{49}$Ar		
(keV)	$I_i/10^3$	$\frac{I_i}{I_{1340}}$	$\frac{I_i}{I_{1050}}$	$I_i/10^3$	$\frac{I_i}{I_{1340}}$	$\frac{I_i}{I_{1050}}$
198(3)	1.68(9)	0.65(6)	3.55	3.51(15)	0.40(2)	0.60
1050(29)	0.47(11)	0.18(4)	1.	5.84(24)	0.67(4)	1.
1266(41)	0.75(17)	0.29(7)	1.59	1.42(29)	0.16(3)	0.24
1340(14)	2.58(19)	1.	5.45	8.73(33)	1.	1.50
1466(21)	1.22(14)	0.47(7)	2.58	1.02(22)	0.12(3)	0.17

The inelastic scattering channel ^{49}Ar(p, p') is shown in Fig. 2(c). In order to display all the statistics for high-energy photons, the vertex reconstruction was not used here. The low-energy background subtraction procedure with the unreacted beam, used for all the other channels, could not be applied in this case. In spite of the dominance of the low energy component below 500 keV and low statistics above, there is evidence for γ rays with energies larger than 800 keV. We see that two response functions corresponding to the transitions at 1340 and 1466 keV observed previously may explain the high energy part around 1400 keV. The region between 700 and 1200 keV is more uncertain due to either (*i*) a possible tail of the low-energy background not fully reproduced, (*ii*) the contribution of the transition at 1050 keV, or (*iii*) decays of unresolved collective states populated in the scattering. At this step, we can only say that these transitions originate from the decay of states populated by collective nuclear excitations from the ground state. An example is proposed in the shell-model calculation using the SDPF − MU$_s$ interaction [46] with the $3/2^-_1 \rightarrow 7/2^-_1$ excitation and the largest value $B(E2)\uparrow = 103\ e9^2\ \mathrm{fm}^4$ obtained for $E2$ excitation from the $3/2^-_1$ ground state. Finally, with limited statistics, the minimal assumption of three response functions at 1050, 1340, and 1466 keV over the low-energy background is enough to reproduce data in Fig. 2(c).

C. Momentum distributions

Due to the large acceptance of the magnetic spectrometer SAMURAI, most of the charged reaction products and unreacted beams were measured in the detectors used for the reconstruction of momentum distributions, as explained in Ref. [36]. The exclusive parallel (PMD) and transverse p_x (TMD) momentum distributions are seen in Fig. 4 with a 40 MeV/c binning corresponding to the experimental resolution. For each bin, the amplitudes of the response functions from Fig. 2(a) were determined. Then, the distributions were normalized through the experimental cross sections associated with these transitions. For each transition, there is an underlying Compton background in the spectrum from higher-lying response functions and from other unresolved transitions. It may introduce some uncertainty on the intensity of the momentum bin due to possible contributions from other ℓ values, especially for the lowest-energy transitions, such as the 198 keV transition. Due to the limited statistics, momentum distributions could only be determined for the most intense transitions at 198 and 1340 keV.

For the one-neutron knockout channel, these distributions are sensitive to the orbital angular momentum ℓ of the knocked-out nucleon and can be compared to distributions obtained from various reaction models. Besides the popular choice of distorted-wave-impulse-approximation (DWIA) [48,49], we also used the transfer to continuum (TC) method [47], as shown in Fig. 4 for p and f waves, with very similar results. The slight asymmetry observed in parallel momentum distributions is a phase space effect due to energy and momentum conservation [50].

The distributions (a) and (c) obtained for the 198 keV transition are consistent with an $\ell = 1$ knocked-out neutron, narrower than the $\ell = 3$ distribution, in spite of weak possible ℓ background. With only the ℓ value, it was not possible to determine the spin-parity of a 198 keV state, either $3/2^-$ or $1/2^-$, while the theoretical calculations all give energies of the ground and first excited states very close to each other. At variance, the wider distributions (b) and (d) obtained for the 1340 keV transition agreed well with an $\ell = 3$ angular momentum, consistent with the large spectroscopic factor and

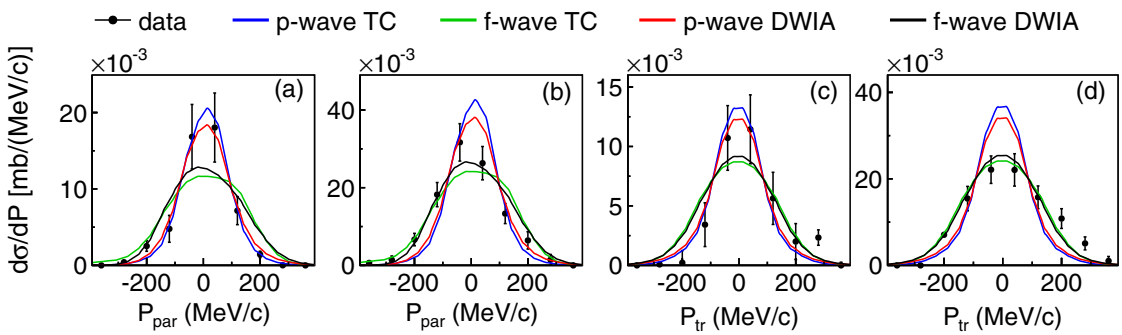

FIG. 4. Momentum distributions of ^{49}Ar ejectiles following the one-neutron knockout reaction: (a) and (b) PMD in coincidence with the 198 and 1340 keV transitions measured in DALI2$^+$; (c) and (d) TMD in coincidence with the 198 and 1340 keV transitions. Data are compared to calculations with the TC [47] and DWIA [48] methods for $\ell = 1$ and $\ell = 3$ waves after convolution with the experimental resolution.

TABLE II. Comparison between experimental results and theoretical predictions derived from shell-model calculations with the SDPF − MU$_s$ interaction [46] for the one-neutron knockout reaction ^{50}Ar(p, pn). The excitation energies $E_{\rm exp}$, cross sections $\sigma_{\rm exp}$, and angular momentum transfer $\Delta\ell$ for the listed states in ^{49}Ar are deduced from the experiment. Theoretical cross sections $\sigma_{{\rm th},i}$ are obtained from Eq. (1), using the calculated C^2S spectroscopic factors and single-particle cross sections $\sigma_{\rm sp}^{lj}(E^*, E_{\rm inc})$ from the TC [47] and DWIA [48] methods. The states are listed up to the estimated one-neutron separation energy 2780(400) keV [42]. The last three rows compare the total inclusive cross section $\sigma_{\rm inc}$ to the sum of exclusive experimental cross sections $\sum\sigma_i^{\rm ex}$ and the sum of theoretical cross sections $\sum\sigma_{{\rm th},i}$.

Experiment			$\sigma_{\rm sp}^{lj}(E^*, E_{\rm inc})$			SDPF-MUs				
$E_{\rm exp}$ (keV)	$\sigma_{\rm exp}$ (mb)	$\Delta\ell$	nlj	$\sigma_{\rm TC}$ (mb)	$\sigma_{\rm DW}$ (mb)	State	Energy (keV)	C^2S	$\sigma_{\rm th,TC}$ (mb)	$\sigma_{\rm th,DWIA}$ (mb)
gs	<17(3)		$1p_{3/2}$	7.4	7.94	$3/2_1^-$	gs	1.844	13.64	14.64
198(3)	3.0(9)	1	$1p_{1/2}$	7.2	7.53	$1/2_1^-$	94	0.616	4.43	4.64
1050(29)	1.5(3)			5.8	4.69	$5/2_1^-$	923	0.006	0.03	0.03
1340(14)	8.3(7)	3	$0f_{7/2}$	6.1	5.52	$7/2_1^-$	983	2.564	15.64	14.15
1466(21)	6.3(10)		$1p_{3/2}$	6.4	7.15	$3/2_2^-$	1197	0.678	4.34	4.85
			$0f_{5/2}$	5.9	4.59	$5/2_2^-$	1460	0.233	1.37	1.07
			$0f_{5/2}$	5.7	4.49	$5/2_3^-$	2096	0.019	0.11	0.08
			$1p_{3/2}$	5.7	4.47	$3/2_3^-$	2184	0.029	0.16	0.13
						$9/2_1^-$	2267	0		
			$0f_{7/2}$	5.9	5.21	$7/2_2^-$	2317	0.050	0.29	0.26
			$1p_{1/2}$	5.8	6.22	$1/2_2^-$	2529	0.017	0.10	0.11
			$0f_{7/2}$	5.8	5.14	$7/2_3^-$	2702	0.262	1.52	1.35
			$1p_{3/2}$	5.85	6.37	$3/2_4^-$	2870	0.191	1.12	1.22
						$9/2_2^-$	3044	0		
			$1p_{1/2}$			$1/2_3^-$	3094	0.000		
$\sigma_{\rm inc}$	36.3 (9)							$\sum\sigma_{{\rm th},i}$	42.75	42.53
$\sum\sigma_{{\rm exp},i}^{\rm ex}$	19.1(18)									

cross section calculated for the $7/2_1^-$ state in Table II. These angular momentum assignments have also been tested with a Bayesian analysis [51]. We find that the $\log_{10}$ scaled Bayes factors are always $\log_{10}(B_{10}) > 8$,[1] such that a p-wave character is preferred over an f-wave one in the 198 keV state distributions; in the 1340-keV state distributions, there is an f-wave over a p-wave character with $\log_{10}(B_{10}) > 6$, which quantitatively supports the ℓ assignment.

For the ground state, we calculate momentum distributions from the difference between the inclusive distribution and the sum of contributions from the most intense transitions at 198 and 1340 keV due to the lack of statistics in each bin for other contributions. The resulting distributions do not allow us to conclude between a pure $\ell = 1$ or $\ell = 3$ character. However, as shown further, all theoretical calculations predict $\ell = 1$ for the ground state of ^{49}Ar.

D. Level scheme

Based on these observations, a tentative level scheme for ^{49}Ar is proposed in Fig. 5.

Except for the $\ell = 1$ value of the first excited state, there is no direct experimental information for the spin-parity assignment of the ground and first excited state. Compared to theoretical calculations, they are consistent with a spin-parity of either $1/2_1^-$ or $3/2_1^-$.

On the basis of momentum distributions, the most intense transition at 1340 keV is assigned to the decay of the $7/2^-$ state, either by $E2$ transition to $3/2^-$ or $E4(M3)$ to $1/2^-$. The prompt character of the observed transition is in favor of a $E2$ transition. Since the intensity of the 1340 keV transition is much larger than the one of the 198 keV transition, we conclude in favor a direct decay by $E2$ transition from a level at 1340 keV to the $3/2_1^-$ ground state, as shown in Fig. 5. The first excited state at 198 keV is proposed to be of spin-parity $1/2_1^-$.

The 1466 keV transition is proposed to be a direct decay to the ground state from the $3/2_2^-$ state, present in theoretical calculations with a single-particle character. A decay to the first excited $1/2_1^-$ state is proposed through 1266 keV transition. The branching ratio obtained from the intensity ratio of the two transitions, I_{1466}/I_{1266}, is expected to be the same in the two different reaction channels, one-neutron knockout and multinucleon removal. Due to the overwhelming transition at 1340 keV, there is a strong uncertainty on the intensity of the transition at 1266 keV, which could partly explain the difference of 1.6(4) for the one-neutron knockout and 0.7(2) for the other channel, when the amplitude of response functions are free parameters of the fit. Alternatively, a ratio fixed to 1.6 could also provides a good reproduction of Fig. 2(b) with only a small increase of the χ^2 value. Unresolved small contributions, possibly coming from cascade decays of $5/2_2^-$

[1]Bayes factors provide decisive evidence for one model when compared to another model if their $\log_{10}(B_{10})$ is larger than 2.

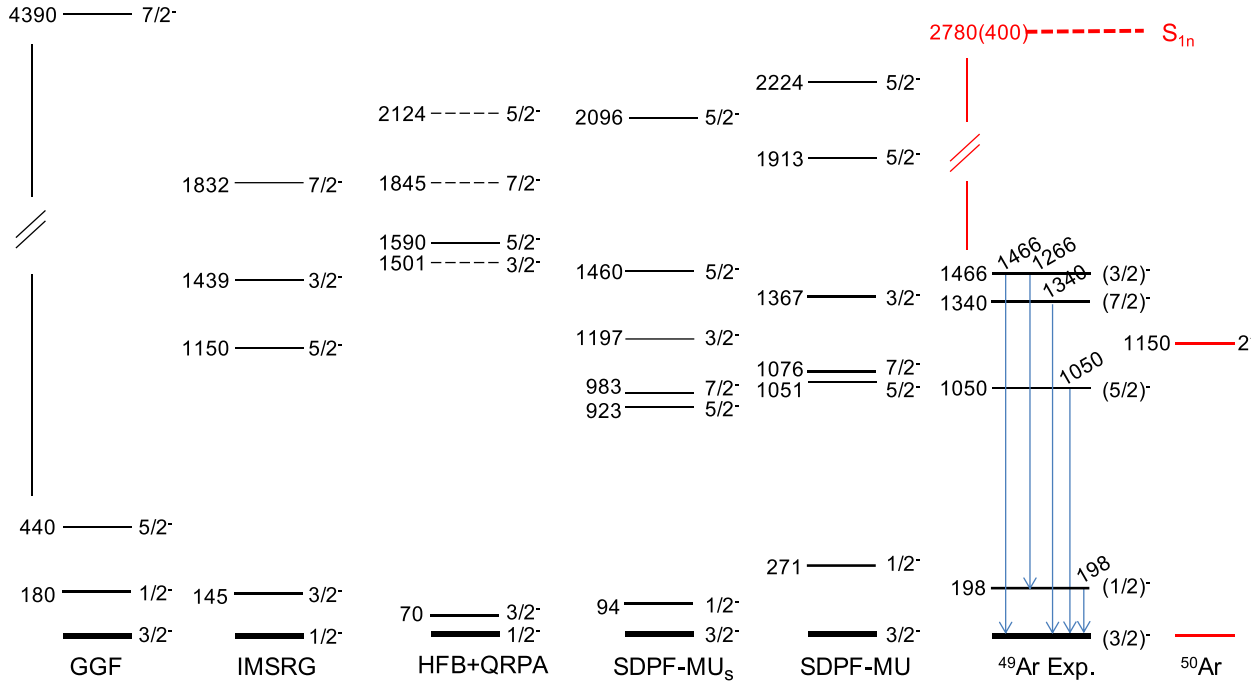

FIG. 5. Level scheme of ^{49}Ar with excitation energies expressed in keV. Experimental results (right) are obtained from the analyses of Fig. 2. They are compared to the theoretical calculations developed in the text: from right to left, shell-model calculations performed with the SDPF − MU$_s$ and the original SDPF-MU interactions, energy-density functional calculations including states obtained from the quasiparticle random phase approximation (QRPA, dashed lines), IMSRG calculation with the EM 1.8/2.0 interaction, and GGF calculation with the $NN + 3N$(lnl) interaction; ^{50}Ar is shown on the right side with the latest $E(2_1^+)$ value taken from [29].

or $7/2_3^-$, might also play a role that calls for a better γ-ray energy resolution.

For the last transition observed at 1050 keV, we have no strong experimental proposition, except that the theoretical calculations predict a $5/2_1^-$ state at nearby excitation energy and quite a small spectroscopic factor. It is consistent with a weak direct population in the one-neutron knockout, while it could be fed by unresolved high spin states populated in the multinucleon removal, such as the $5/2_2^-$ state.

E. Cross sections

Inclusive and exclusive cross sections have been calculated using the same prescriptions detailed in Ref. [36]. The only difference comes from the value of the efficiency for the detection of one proton in the MINOS setup $\varepsilon_{\rm MINOS} = 0.71(2)$, which has been used here for the ^{50}Ar(p, pn) channel. This value is consistent with other (p, pn) analyses with the MINOS setup, such as those in [16,45].

Before subtraction, the contribution from the inelastic scattering channel ^{50}Ar$(p, p')^{50}$Ar decaying to ^{49}Ar was determined to be 4.8% of the total events, predominantly in the population of states leading to the 198 keV (6.4%), 1050 keV (15.5%), and 1340 keV (3.9%) transitions.

Intensity values of 5.4(3), 1.5(3), 2.4(5), 8.3(7), and 3.9(5) mb were determined for the 198, 1050, 1266, 1340, and 1466 keV transitions, respectively. According to the level scheme shown in Fig. 5, we obtained the experimental exclusive cross sections $\sigma_{\rm exp}$ for the direct population of states in the ^{50}Ar$(p, pn)^{49}$Ar knockout displayed in Table II.

Due to the Doppler shift, the transition at 198 keV spreads downwards in energy for detectors placed in the backward direction in the laboratory frame. The possible impact of the energy threshold has been checked by selecting a set of detectors corresponding to the three first layers in the forward direction of DALI2$^+$, as shown in Ref. [52]. The obtained cross sections are compared to values for the full ensemble of DALI2$^+$: 5.39(33) and 4.99(38) mb for the transition at 198 keV, respectively. The same was done for the transition at 1340 keV with 8.26(66) and 7.39(72) mb. There is no evidence of an impact within the error bars and no difference with the 1340 keV transition for which no impact is expected.

Experimental values are compared to the results of cross section calculations $\sigma_i^{\rm ex}(E^*)$ for excitation energies E^* at a given incident energy $E_{\rm inc}$ following

$$\sigma_i^{\rm ex}(E^*) = \sum_{l,j} C^2S^i_{l,j}\,\sigma^{lj}_{\rm sp}(E^*, E_{\rm inc}), \qquad (1)$$

where the theoretical spectroscopic factors $C^2S^i_{l,j}$ are multiplied by the single-particle cross sections $\sigma^{lj}_{\rm sp}(E^*, E_{\rm inc})$ obtained in a reaction model. Here, they were calculated with the TC [47] and DWIA [48] methods at 217 MeV/nucleon, which corresponds to the mid-target energy for ^{50}Ar projectiles. Values are given in Table II and used in the calculation of $\sigma_{\rm th}$ for the predicted states below the one-neutron separation energy. An overall agreement is observed with experimental values, except for the large value predicted for the population of the $7/2_1^-$ state, which possibly suggests a smaller spectroscopic factor.

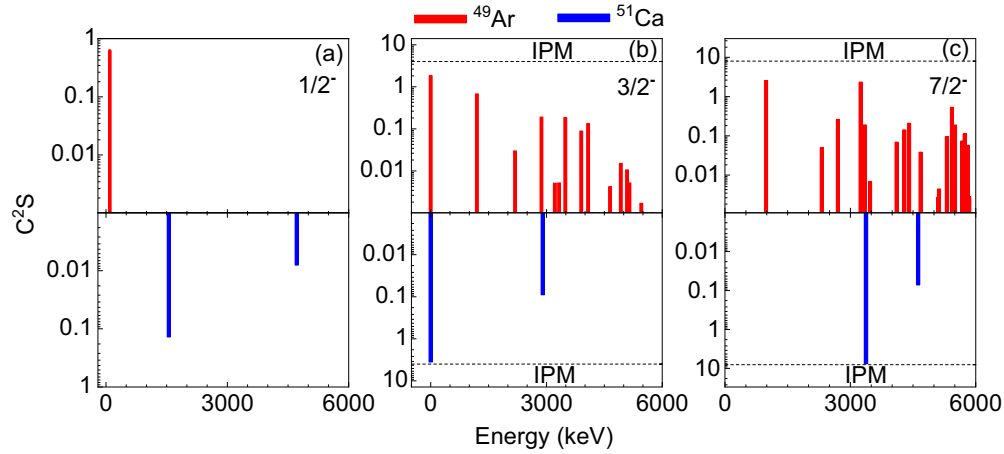

FIG. 6. Spectroscopic factor $||\langle^{A-1}X + n||^AX\rangle||^2$ distributions for (a) $1/2^-$, (b) $3/2^-$, and (c) $7/2^-$ states in ^{49}Ar (red) and ^{51}Ca (blue) obtained in the shell-model calculation with the SDPF-MUs interaction [46]. The dashed line corresponds to the maximal occupancy $2j + 1$ of the corresponding neutron orbitals $\nu 1p_{3/2}$ and $\nu 0f_{7/2}$ in an independent particle model (IPM).

The inclusive cross section was determined to be $\sigma_{\rm inc} = 36.3(9)$ mb. The cross section to populate the ground state was calculated as the difference between the inclusive cross section and the sum of the exclusive cross sections for transitions known to feed the ground state. This prescription is valid as long as the feeding from unresolved higher-lying states is negligible. This is a first-order approximation, reasonable considering the low value of the one-neutron separation energy S_n. However, in the list of higher-lying states predicted in the SDPF-MUs calculation, states such as $5/2^-_2$ or $7/2^-_3$ could partly populate the ground state with non-identified weak transitions. Therefore, the result of 17.2 mb has to be considered as an upper limit for σ_{gs}.

Overall consistency may be tested through the reduction factor $R_s = \sigma_{\rm inc}/\sum\sigma_{{\rm th},i}$, using the spectroscopic factor predictions of a shell model routinely used in this region like SDPF-MUs calculation in Tables II. The value $R_s = 0.85(2)$ is found with the TC and DWIA reaction models, which places ^{50}Ar(p, pn) ($\Delta S = -17.8$ MeV) in the general trend observed for the one nucleon knockout reactions (see Ref. [53] and Fig. 2 in Ref. [54]).

IV. DISCUSSION

In the following, the $N = 32$ neutron number is investigated for ^{50}Ar, together with the reference nucleus ^{52}Ca. Properties of the even-even nuclei, as well as the $N - 1$ ones obtained from the one-neutron knockout, are discussed with the help of different theoretical methods.

First, shell-model calculations were performed using different versions of the SDPF-MU interaction, which were tuned to reproduce data in this mass region. Additional insight on excited states and the quadrupole deformation degree of freedom is then provided via Hartree-Fock-Bogoliubov (HFB) calculations based on the D1M parametrization [55] of the Gogny effective interaction [56]. Finally, new results from valence-space and full-space *ab initio* approaches are also provided to complete the theoretical analysis. Some of these theoretical tools were already employed in Ref. [36], where details about the computational schemes can be found.

The computed low-lying spectra using these methods are displayed in Fig. 5. Other theoretical results are shown in Figs. 6–8, while numerical values are given in Tables III to VI in the text and in the Appendix.

A. Shell-model calculations

The shell-model calculations were performed with the SDPF-MUs interaction, which was derived from the original SDPF-MU interaction [57] and tuned to improve the results for K and Ca isotopes [46]. This tuning was useful to reproduce the excitation energy of the first 2^+ state in argon isotopes up to ^{52}Ar [27]. However, the level scheme in Fig. 5 is better reproduced with the original SDPF-MU interaction. A slightly larger compression is observed with SDPF-MUs, with nevertheless the same level ordering.

In a shell-model picture, one would expect, for a closed-shell nucleus at $N = 32$ in a spherical configuration, the $\nu 0f_{7/2}$ and $\nu 1p_{3/2}$ orbitals to be filled and $\nu 1p_{1/2}$ and $\nu 0f_{5/2}$ orbitals to be empty. The numerical values for the neutron content N_ν of the ^{52}Ca and ^{50}Ar orbitals are displayed in Table III. The $\nu 1p_{3/2}$ and $\nu 0f_{7/2}$ orbitals are slightly emptied in ^{50}Ar compared to the closed shell isotone ^{52}Ca, with a corresponding increase for the $\nu 1p_{1/2}$ and $\nu 0f_{5/2}$ orbitals. The relative effect is quite strong for $\nu 1p_{1/2}$. This change

TABLE III. Neutron content N_ν of the different fp orbitals in the gs wave function of ^{52}Ca and ^{50}Ar obtained in the shell-model calculation using the SDPF-MUs interaction.

$N_\nu(nlj)$	^{52}Ca	^{50}Ar
$\nu 0f_{7/2}$	7.95	7.61
$\nu 0f_{5/2}$	0.13	0.41
$\nu 1p_{3/2}$	3.76	3.28
$\nu 1p_{1/2}$	0.17	0.70

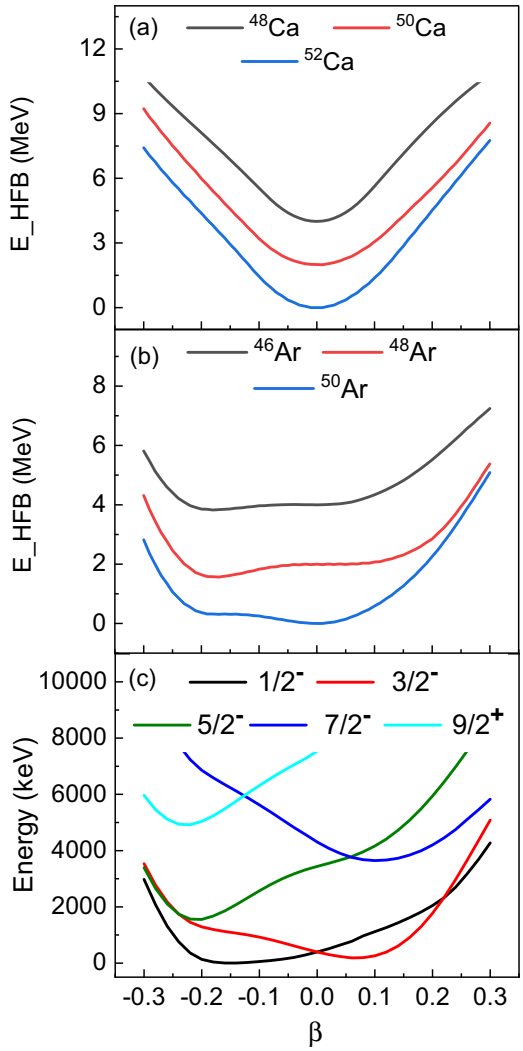

FIG. 7. Potential energy surfaces energy E_{HFB} versus the quadrupole deformation parameter β for argon (a) and calcium (b) isotopes obtained from HFB calculations based on the D1M parametrization [55] of the Gogny effective interaction [56]. The curves are shifted by 2 MeV from each other in order to allow superposition. (c) HFB + blocking calculations (see text) for the lowest-lying states of ^{49}Ar at a given spin-parity $1/2^-$, $3/2^-$, $5/2^-$, $7/2^-$, and $9/2^+$.

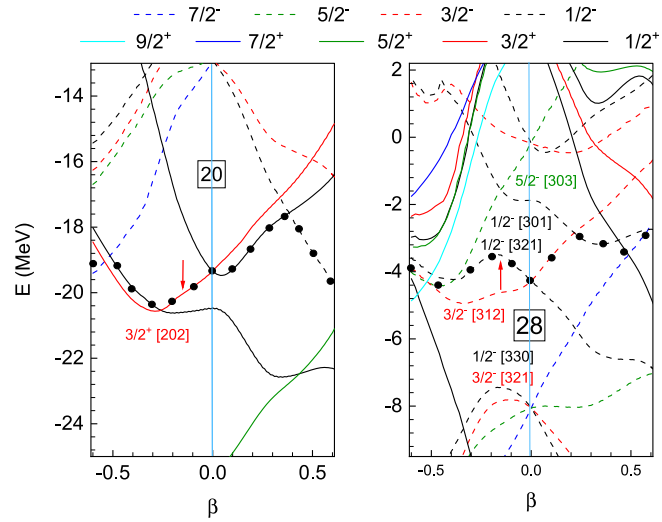

FIG. 8. Energy of the proton (left) and neutron (right) orbitals versus the quadrupole deformation β parameter in ^{50}Ar obtained from Hartree-Fock-Bogoliubov (HFB) calculations based on the D1M parametrization [55] of the Gogny effective interaction [56]. The orbitals discussed in the text are labeled with the usual Nilsson parameters $K[N, n_z, \Lambda]$. The black dots stand for the Fermi level. The red arrow is placed at $\beta = -0.15$.

is not driven by the monopole gap between the $\nu 1p_{3/2}$ and $\nu 1p_{1/2}$ orbitals, which do not significantly change from one nucleus to the other, as already mentioned in Ref. [28]. At the same time, more mixing is predicted in Table IV for the wave function of the ^{50}Ar ground state, compared to ^{52}Ca. The SDPF-MU calculation in Ref. [29] also predicts for ^{50}Ar a ratio $E(4_1^+)/E(2_1^+) = 2.05$, consistent with a vibrational character. This is the first indication of collective effects present in ^{50}Ar.

The one-neutron knockout ^{50}Ar(p, pn) is a good tool to test the persistence of the shell effect observed at $N = 32$ on ^{52}Ca, as recently obtained for ^{52}Ca(p, pn) [16]. Without correlations, the occupancy number should be found at $2j + 1$ for fully occupied orbitals and 0 for empty ones. The spectroscopic factor C^2S distributions calculated for the low-lying $1/2^-, 3/2^-$and $7/2^-$ states in ^{49}Ar and ^{51}Ca are shown in Fig. 6.

$3/2^-$ states.. The C^2S value for the $3/2_1^-$ ground state in ^{51}Ca is very close to the $2j + 1$ value, which is a signature of a single-particle character with a strong overlap with a neutron hole in the $\nu 1p_{3/2}$ orbital in ^{52}Ca. In ^{49}Ar and in spite of the high excitation energy range, the sum $\sum_i (C^2S)_i = 3.19$ is still lower than the value for $3/2_1^-$ in ^{51}Ca, with evidence for a fragmentation of the distribution. The shell-model calculation predicts a $3/2_1^-$ ground state for ^{49}Ar. It also predicts a $3/2_2^-$ state at 1197 keV with a significant spectroscopic factor, which we assume to be consistent with the 1466 keV state in Fig. 5 and the measured cross sections. Higher-lying states are also predicted, such as $3/2_4^-$ at 2870 keV very close to the estimated S_n value. If not unbound, they will be part of the feeding to lower-lying states.

$1/2^-$ states. The $1/2_1^-$ state in ^{51}Ca has a large excitation energy at about 1.5 MeV and a small spectroscopic factor. This is consistent with a weak population of the $\nu 1p_{1/2}$ orbital in ^{52}Ca, such as the removal of a $1p_{1/2}$ neutron from a

TABLE IV. 0p0h and 2p2h components of the wave function for the lowest two 0^+ of ^{52}Ca and ^{50}Ar, obtained in the shell-model calculation using the SDPF-MU interaction.

	Energy (keV)	0p0h (%)	2p2h (%)
^{52}Ca 0_1^+	gs	87.1	12.4
^{52}Ca 0_2^+	4007	7.3	88.9
^{50}Ar 0_1^+	gs	54.0	28.8
^{50}Ar 0_2^+	2412	25.4	58.5

$(\nu 1p_{3/2})^2(\nu 1p_{1/2})^2$ configuration with a small weight in the ^{52}Ca wave function and a large $\nu 1p_{3/2}$-$\nu 1p_{1/2}$ spherical gap. This is what is expected for a closed shell nucleus at $N = 32$ in the shell-model framework. A very different conclusion may be drawn for ^{49}Ar. The energy difference between the ground and the first excited state is found to be quite small in many calculations. The shell-model calculation with the SDPF-MUs interaction predicts the $1/2^-_1$ state at 94 keV. A comparably small value is obtained with the original SDPF-MU interaction. Whereas the C^2S value for $3/2^-_1$, although large, is well reduced compared to the ^{51}Ca case, the C^2S value for $1/2^-_1$ significantly increases from ^{51}Ca to ^{49}Ar. The experimental cross section measured for the first excited state in ^{49}Ar, assumed to be $1/2^-_1$, is consistent with the large value C^2S calculated with the SDPF-MUs interaction in Table II. Both the low excitation energy and the substantial C^2S value of the $1/2^-_1$ state are clear indications of collective effects present in ^{49}Ar.

$5/2^-$ *states.* A $5/2^-_1$ state is found in most of the calculations around 1 MeV, which supports the assumption of such a state at 1050 keV in Fig. 5. It is weakly populated in the neutron knockout reaction, as expected from the small value of the spectroscopic factor displayed in Table V. A large value $B(E2; 5/2^-_1 \rightarrow 1/2^-_1) = 177\ e^2\text{fm}^4$ is also predicted.

$7/2^-$ *states.* Here again ^{51}Ca and ^{49}Ar are found to be quite different. There is mainly one low-lying $7/2^-$ state in ^{51}Ca, around 3 MeV with a large C^2S value, very close to the $2j + 1$ limit in Fig. 6(c). This strong overlap is consistent with a neutron hole in the $\nu 0f_{7/2}$ orbital in ^{52}Ca. In ^{49}Ar, in spite of the high excitation energy range, the sum $\sum_i (C^2S)_i = 6.95$ is still lower than the value for $7/2^-_1$ in ^{51}Ca, with evidence for a fragmentation of the distribution. Two states, $7/2^-_1$ and $7/2^-_4$, have a large C^2S value. The origin of the calculated $7/2^-_4$ state can be easily understood since its excitation energy is predicted to be 3245 keV, very similar to the value obtained for $7/2^-_1$ in ^{51}Ca. It can therefore be associated with the neutron removal from the spherical $\nu 0f_{7/2}$ orbital. The excitation energy of such a state is well above the one-neutron separation energy S_n. This calls for invariant mass reconstruction, which will not be discussed here.

The $7/2^-_1$ state seems more complex, with a low excitation energy $E^* = 983$ keV and a large value $B(E2; 7/2^-_1 \rightarrow 3/2^-_1) = 144.2\ e^2\text{fm}^4$ to the ground state. In the shell-model framework, it is tempting to link it with a more complex neutron configuration in ^{50}Ar, involving some $\nu(1p_{3/2})^2(1p_{1/2})^2$ components compared to $\nu(1p_{3/2})^4$, already encountered for the population of the $1/2^-_1$ state. Its energy is also close to the 2^+_1 state excitation energy in ^{50}Ar, which suggests a vibrational component for a state built on the $3/2^-_1$ ground state.

With small C^2S values, the $7/2^-_2$ and $7/2^-_3$ states are weakly populated in the one-neutron knockout. Moreover, they do not directly decay to the ground state, feeding states at lower excitation energy in a complex decay pattern.

B. Energy-density functional calculations

The analysis is complemented with results of energy-density functional calculations based on the D1M parametrization [55] of the Gogny effective interaction [56]. The potential energy surfaces (PES) are shown in Fig. 7 for calcium and argon isotopes. While the calcium isotopes are found to be spherical, PES are much softer for argon isotopes and a trend towards oblate deformation is observed, favored by the gain in energy for the $3/2^+[202]$ proton orbital, as observed in Fig. 8 (left panel). This results in a competition between the spherical minimum and an oblate configuration around $\beta \simeq -0.2$. At the mean-field level, permanent oblate deformation is predicted for ^{48}Ar, but ^{50}Ar remains spherical.

In the present HFB calculations assuming axial symmetry around the z axis, the low-lying states in ^{49}Ar are described within the blocking approximation by a one-quasiparticle (qp) excitation on top of a qp vacuum. Along the binding energy minimization process, the occupation probability of the one-qp orbital is imposed. This orbital is selected according to its quantum numbers and numbering by its qp energy, i.e., with respect to the Fermi level. Odd-A HFB states with spin-parity J^π are obtained by selecting qp orbitals with angular momentum projection and parity $K^\pi = J^\pi$. On top of the HFB with K blocking calculations, vibrational states are described within a consistent QRPA approach. More details can be found concerning the HFB and HFB + QRPA approaches in Refs. [58,59] for the treatment of odd systems. The minimization of the lowest energy states with parity $1/2^-$ to $7/2^-$ and $9/2^+$ versus the quadrupole deformation is shown in Fig. 7.

The D1M mean-field ground state is obtained by blocking on the first $K = 1/2$ quasiparticle orbital, with a soft oblate minimum at $\beta = -0.15$. It is consistent with the neutron knockout from the valence orbital $1/2^-[321]$ in ^{50}Ar at moderate oblate deformation. Here again, the $1/2^-_1$ and $3/2^-_1$ states are very close to each other, but $3/2^-_1$ is found as a nearly spherical excited state at 70 keV. The next $3/2^-$ state is found by blocking at much higher energy around 3350 keV. Therefore, the experimental $3/2^-_2$ state at 1466 keV seems to be more consistent with a collective state, at about the same energy as the 2^+_1 state in ^{50}Ar.

Blocking the first $K = 5/2$ qp orbital, the $5/2^-_1$ state is found at 1590 keV above the $1/2^-$ HFB minimum and an oblate deformation $\beta = -0.20$. It is partly associated with the $K = 5/2$ orbital of $\nu 0f_{5/2}$ parentage, $5/2^-[303]$ in Fig. 8 (right panel), which is strongly favored by the oblate deformation. Another origin could be a collective state, such as a vibrational $K = 2$ state built on top of the $1/2^-_1$ state.

Blocking the $K = 7/2$ qp orbital, no $7/2^-$ state is obtained below 3 MeV. The first $7/2^-$ state is found at 3650 keV with a small prolate deformation $\beta_2 = +0.1$. It is closely related to the $7/2^-[303]$ orbital, with a nearly pure wave function. This suggests that the experimental $7/2^-_1$ state at 1340 keV in Fig. 5 could partly be a vibrational one. From QRPA calculations performed for phonons acting on the odd QRPA ground state $J = 3/2^-$, the experimental state might be a mixing of the three QRPA states obtained for the $K = 0$, 1, and 2 phonons, the main component being the QRPA state for the $K = 0$ at 1775 keV.

This discussion, based on shell-model calculations as well as an energy-density functional approach, is consistent with a sharp transition from a spherical configuration at $N = 32$ when protons are removed from ^{52}Ca to ^{50}Ar. A low-lying

$1/2^-$ state in ^{49}Ar, as well as $7/2^-$ and $3/2^-$ states at excitation energies close to the first 2_1^+ state in ^{50}Ar, may be assigned to the existence of collective effects. This evolution is now also been investigated with the help of recently developed *ab initio* approaches.

C. *Ab initio* calculations

Ab initio calculations were performed in the context of the valence-space in-medium similarity renormalization group (VS-IMSRG) [60] and the self-consistent Gorkov Green's function (GGF) [61,62] approaches.

In the VS-IMSRG approach, the *sd* and the full *pf* shells above a ^{28}O core were considered for proton and neutron valence spaces, respectively. Three-nucleon forces between valence nucleons were captured via ensemble normal ordering [63]. Calculations were performed within 15 major oscillator shells, whereas an additional cut on three-nucleon configurations was introduced at $E_{3\mathrm{max}} = 24$ [64]. The spectroscopic factors were computed with the bare annihilation operators, although ideally, they should be evolved consistently with the Hamiltonian. The consistent evolution would change the spectroscopic factor by roughly 10% [65]. The two- plus three-nucleon 1.8/2.0 EM interaction [66] was employed throughout the study.

VS-IMSRG predictions for low-lying states are similar to the ones from the SDPF-MUs calculation, with two main exceptions. First, a less compressed level scheme is found for ^{49}Ar, as is visible from Fig. 5. Moreover, a spin inversion for the ground state ($1/2_1^-$ instead of $3/2_1^-$) is predicted, although the two states are very close to each other in excitation energy. This spin inversion is also observed in VS-IMSRG calculations performed with other interactions, such as $\Delta\mathrm{NNLO_{GO}}$ [67] or $NN + 3N(\mathrm{lnl})$ [68].

GGF calculations were performed in the *A*-body Hilbert space truncated to 14 major oscillator shells, with a further cut on three-nucleon matrix elements imposed by $E_{3\mathrm{max}} = 16$. Although the latter is smaller than the one introduced in VS-IMSRG calculations, it is sufficient to converge all relevant observables. Two different interactions were employed, namely $\mathrm{NNLO_{sat}}$ [69] and $NN + 3N(\mathrm{lnl})$ [68]. As for the other theoretical approaches, the properties of the low-lying states in ^{51}Ca suggest that ^{52}Ca is a closed-shell nucleus: (*i*) large C^2S values close to the $2j + 1$ limit for the $3/2_1^-$ ground state and $7/2^-$ fragment are found at high excitation energy for both interactions; (*ii*) the first $1/2^-$ state appears at high excitation energy, especially with $\mathrm{NNLO_{sat}}$, and has very small C^2S values.

In contrast, corresponding results for ^{49}Ar point to the emergence of a qualitatively different picture. The C^2S values for the main $3/2^-$ and $7/2^-$ states decrease, although the change is quantitatively different with the two interactions. While the reduction is significant (around 30%) for $NN + 3N(\mathrm{lnl})$, only a ≈5–10% decrease is observed for $\mathrm{NNLO_{sat}}$. This is presumably due to the fact that the former interaction predicts consistently smaller $0d_{3/2}$-$1s_{1/2}$ proton gaps, hence favoring more fragmentation in spite of being sensibly more perturbative of NNLOsat. Contrarily to valence-space calculations, here, the energy of the $7/2^-$ state changes by only a few hundred keV, and a component below 1 MeV is not observed for this angular momentum. Importantly, together with the reduction of spectroscopic factors, a low-energy $1/2^-$ state appears with both interactions. In addition, the energy of the first $5/2^-$ state is lowered by more than 1 MeV. These features all signal an increase of collectivity in ^{49}Ar.

Altogether, the changes observed in GGF calculations when going from ^{51}Ca to ^{49}Ar are consistent with shell-model results and point to the deterioration of the $N = 32$ gap in argon. The quantitative differences emerging in the two sets of results are very likely due to the missing collective degrees of freedom (i.e., lack of deformation and low truncation in the particle-hole expansion) in the GGF approach.

V. CONCLUSIONS

In summary, the one-neutron knock-out $^{50}\mathrm{Ar}(p, pn)$ reaction was studied in inverse kinematics on a thick liquid hydrogen target at about 217 MeV/u. The spectroscopy of ^{49}Ar was obtained by fast in-beam γ-ray measurements with the help of the DALI2$^+$ array for transitions from low-lying bound states. A first level scheme could be proposed for ^{49}Ar, with tentative assignment of spin parities for the $1/2_1^-$ and $7/2_1^-$ excited states.

The resulting low-energy spectroscopy of ^{49}Ar and cross sections, in addition to the spectroscopic factors obtained in theoretical calculations, are consistent with a description more complex than that used for ^{51}Ca, as illustrated by the PES in HFB calculations. While a spherical configuration, expected from the $N = 32$ shell closure, is still present in ^{49}Ar for some states (such as the $3/2_1^-$ ground state or the $7/2_4^-$ state in the SDPF-MUs calculation), one also observes the onset of collective effects consistent with quadrupolar deformation or vibration. In particular, this is manifested by the low excitation energy and substantial C^2S values of the $1/2_1^-$ state. Interestingly, this collective character is not driven by a reduction of the $N = 32$ gap, which roughly remains constant when going from calcium to argon. *Ab initio* calculations also consistently predict an increase of collectivity in ^{49}Ar as compared to ^{51}Ca. This is indicated by the appearance of low-energy states in the excitation spectrum as well as a significantly more fragmented strength in argon. In the future, it will be interesting to further investigate these findings in the ^{48}S isotone, for which the proton valence orbital from $\pi 1s_{1/2}$ parentage has a very different dependence on quadrupole deformation.

ACKNOWLEDGMENTS

We thank the RIKEN Nishina Center accelerator staff for their work in the primary beam delivery and the BigRIPS team for preparing the secondary beams. The development of MINOS has been supported by the European Research Council through the ERC Grant No. MINOS258567. B.D.L. and L.X.C. acknowledge support from the Vietnam Ministry of Science and Technology under Grant No. ĐTCB.01/21/VKHKTHN. M.G.-R. and A.M.M. acknowledge financial support by MCIN/AEI/10.13039/501100011033 under I + D + i Project No. PID2020-114687GB-I00 and under Grant

No. IJC2020-043878-I (also funded by "European Union NextGenerationEU/PRTR"), by the Consejería de Economía, Conocimiento, Empresas y Universidad, Junta de Andalucía (Spain) and "ERDF-A Way of Making Europe" under PAIDI 2020 Project No. P20_01247, and by the European Social Fund and Junta de Andalucía (PAIDI 2020) under Grant No. DOC-01006. T.M. acknowledges the European Research Council (ERC) under the European Union's Horizon 2020 research and innovation program (Grant Agreement No. 101020842) F.B. was supported by the RIKEN Special Postdoctoral Researcher Program. Y.L.S. acknowledges the support of a Marie Skłodowska-Curie Individual Fellowship (H2020-MSCAIF-2015-705023) from the European Union. I.G. was supported by HIC for FAIR and Croatian Science Foundation. R.-B.G. is supported by the Deutsche Forschungsgemeinschaft (DFG) under Grant No. BL 1513/1-1. K.I.H., D.K., and S.Y.P. acknowledge support from an IBS grant funded by the Korean government (No. IBS-R031-D1). P.K. and V.W. were supported in part by the BMBF Grants No. 05P19RDFN1, No. 05P21RDFN1, and No. HGS-HIRe. D.So. was supported by the National Research, Development and Innovation Fund of Hungary via Projects No. K128947 and No. TKP2021-NKTA-42. P.-A.S. acknowledges support from BMBF under Grant No. NuSTAR.DA 05P15RDFN1 and Contract No. PN 23.21.01.06 sponsored by the Romanian Ministry of Research, Innovation and Digitalization. This work was supported in part by JSPS KAKENHI Grants No. JP16H02179, No. JP18H05404, and No. JP20K03981. J.D.H. acknowledges support from NSERC, the National Research Council Canada, and the Arthur B. McDonald Canadian Astroparticle Physics Research Institute. T.M. acknowledges support from the Deutsche Forschungsgemeinschaft (DFG, German Research Foundation), Project-ID 279384907–SFB 1245. This work was supported by the Office of Nuclear Physics, U.S. Department of Energy, under Grant No. de-sc0018223 (NUCLEI SciDAC-4 Collaboration) and the FieldWork Proposal No. ERKBP72 at Oak Ridge National Laboratory (ORNL). Computer time was provided by the Innovative and Novel Computational Impact on Theory and Experiment (INCITE) program. This research used resources of the Oak Ridge Leadership Computing Facility located at ORNL, which is supported by the Office of Science of the Department of Energy under Contract No. DE-AC05-00OR22725. GGF calculations were performed by using HPC resources from GENCI-TGCC (Contracts No. A0090507392 and No. A0110513012) and at the DiRAC DiAL system at the University of Leicester (funded by the UK BEIS via STFC Capital Grants No. ST/K000373/1 and No. ST/R002363/1 and STFC DiRAC Operations Grant No. ST/R001014/1) and at the National Energy Research Scientific Computing Center (NERSC), a U.S. Department of Energy User Facility using Awards No. NP-ERCAP0020946 and No. NP-ERCAP0024959. This work was supported by the United Kingdom Science and Technology Facilities Council (STFC) under Grant No. ST/L005816/1 and in part by the NSERC Grants No. SAPIN-2016-00033, No. SAPIN-2018-00027, and No. RGPAS-2018-522453. TRIUMF receives federal funding via a contribution agreement with the National Research Council of Canada. J.D.H., B.S.H., and T.M. thank S. R. Stroberg for the IMSRG+ + code used to perform the VS-IMSRG calculations [70]. The valence-space diagonalization of the VS-IMSRG calculations were done with the KSHELL code [71]. The VS-IMSRG computations were performed with an allocation of computing resources on Cedar at WestGrid and Compute Canada, and on the Oak Cluster at TRIUMF managed by the University of British Columbia department of Advanced Research Computing (ARC). N.T.T.P is funded by the University of Science, VNU-HCM under Grant No. T2021-02.

APPENDIX

Tables V and VI display the numerical values of the excitation energies and spectroscopic factors for the states populated in the one-neutron knockout from ^{50}Ar and ^{52}Ca obtained in the theoretical calculations given in the main text.

TABLE V. Spin J^π, excitation energies E^*, and spectroscopic factors $||\langle^{A+1}X - n\|^AX\rangle||^2$ for levels of ^{49}Ar and ^{51}Ca obtained in shell-model calculation with the SDPF-MUs interaction and VS-IMSRG calculation with the 1.8/2.0 (EM) interaction [66].

	SM (SDPF-MUs)				VS-IMSRG (1.8/2.0 EM)			
	^{49}Ar		^{51}Ca		^{49}Ar		^{51}Ca	
State	E^* (keV)	C^2S	E^* (keV)	C^2S	E^* (keV)	C^2S	E^* (keV)	C^2S
$3/2^-_1$	gs	1.84	gs	3.57	155	1.37	gs	3.69
$1/2^-_1$	94	0.62	1552	0.14	gs	0.94	2025	0.09
$5/2^-_1$	923	<0.01	2298	<0.01	1150	<0.01	2068	0.00
$7/2^-_1$	983	2.56	3374	7.56	1852	1.89	4197	7.59
$3/2^-_2$	1197	0.68	2893	0.09	1439	0.91	3081	0.06
$7/2^-_2$	2317	0.05	4622	0.07	3271	0.09		

TABLE VI. Spin J^π, excitation energies E^*, and spectroscopic factors $||\langle^{A+1}X - n\|^AX\rangle||^2$ for levels of ^{49}Ar and ^{51}Ca obtained in GGF calculations with the $NN + 3N$(lnl) and NNLO$_{\rm sat}$. interactions. Here we select states for which the spectroscopic factor is larger than 0.01.

	GGF [$NN + 3N$(lnl)]				GGF (NNLO$_{\rm sat}$)			
	^{49}Ar		^{51}Ca		^{49}Ar		^{51}Ca	
State	E^* (keV)	C^2S	E^* (keV)	C^2S	E^* (keV)	C^2S	E^* (keV)	C^2S
$3/2^-$	gs	2.68	gs	3.36	gs	3.17	gs	3.34
$1/2^-$	180	0.22	1610	<0.01	330	0.02	3060	0.03
$5/2^-$	440	0.10	1628	<0.01	1890	<0.01	2980	<0.01
$7/2^-$	3590	0.10	3020	0.02	2480	0.48	4152	0.02
$3/2^-$	3620	0.01	1740	0.02	2690	0.02	3010	0.03
$7/2^-$	4390	3.64	3720	6.75	3980	5.59	4660	6.05

[1] O. Sorlin and M.-G. Porquet, Phys. Scr. **2013**, 014003 (2013).

[2] B. Bastin, S. Grévy, D. Sohler, O. Sorlin, Z. Dombrádi, N. L. Achouri, J. C. Angélique, F. Azaiez, D. Baiborodin, R. Borcea, C. Bourgeois, A. Buta, A. Bürger, R. Chapman, J. C. Dalouzy, Z. Dlouhy, A. Drouard, Z. Elekes, S. Franchoo, S. Iacob *et al.*, Phys. Rev. Lett. **99**, 022503 (2007).

[3] S. Takeuchi, M. Matsushita, N. Aoi, P. Doornenbal, K. Li, T. Motobayashi, H. Scheit, D. Steppenbeck, H. Wang, H. Baba, D. Bazin, L. Càceres, H. Crawford, P. Fallon, R. Gernhäuser, J. Gibelin, S. Go, S. Grévy, C. Hinke, C. R. Hoffman *et al.*, Phys. Rev. Lett. **109**, 182501 (2012).

[4] A. Gade, B. A. Brown, J. A. Tostevin, D. Bazin, P. C. Bender, C. M. Campbell, H. L. Crawford, B. Elman, K. W. Kemper, B. Longfellow, E. Lunderberg, D. Rhodes, and D. Weisshaar, Phys. Rev. Lett. **122**, 222501 (2019).

[5] H. L. Crawford, P. Fallon, A. O. Macchiavelli, P. Doornenbal, N. Aoi, F. Browne, C. M. Campbell, S. Chen, R. M. Clark, M. L. Cortés, M. Cromaz, E. Ideguchi, M. D. Jones, R. Kanungo, M. MacCormick, S. Momiyama, I. Murray, M. Niikura, S. Paschalis, M. Petri *et al.*, Phys. Rev. Lett. **122**, 052501 (2019).

[6] T. Otsuka, R. Fujimoto, Y. Utsuno, B. A. Brown, M. Honma, and T. Mizusaki, Phys. Rev. Lett. **87**, 082502 (2001).

[7] F. Wienholtz, D. Beck, K. Blaum, C. Borgmann, M. Breitenfeldt, R. B. Cakirli, S. George, F. Herfurth, J. D. Holt, M. Kowalska, S. Kreim, D. Lunney, V. Manea, J. Menéndez, D. Neidherr, M. Rosenbusch, L. Schweikhard, A. Schwenk, J. Simonis, J. Stanja *et al.*, Nature (London) **498**, 346 (2013).

[8] S. Michimasa, M. Kobayashi, Y. Kiyokawa, S. Ota, D. S. Ahn, H. Baba, G. P. A. Berg, M. Dozono, N. Fukuda, T. Furuno, E. Ideguchi, N. Inabe, T. Kawabata, S. Kawase, K. Kisamori, K. Kobayashi, T. Kubo, Y. Kubota, C. S. Lee, M. Matsushita *et al.*, Phys. Rev. Lett. **121**, 022506 (2018).

[9] W. S. Porter, E. Dunling, E. Leistenschneider, J. Bergmann, G. Bollen, T. Dickel, K. A. Dietrich, A. Hamaker, Z. Hockenbery, C. Izzo, A. Jacobs, A. Javaji, B. Kootte, Y. Lan, I. Miskun, I. Mukul, T. Murböck, S. F. Paul, W. R. Plaß, D. Puentes *et al.*, Phys. Rev. C **106**, 024312 (2022).

[10] A. Huck, G. Klotz, A. Knipper, C. Miehé, C. Richard-Serre, G. Walter, A. Poves, H. L. Ravn, and G. Marguier, Phys. Rev. C **31**, 2226 (1985).

[11] A. Gade, B. A. Brown, D. Bazin, C. M. Campbell, J. A. Church, D. C. Dinca, J. Enders, T. Glasmacher, M. Horoi, Z. Hu, K. W. Kemper, W. F. Mueller, T. Otsuka, L. A. Riley, B. T. Roeder, T. Suzuki, J. R. Terry, K. L. Yurkewicz, and H. Zwahlen, Phys. Rev. C **74**, 034322 (2006).

[12] S. Chen, F. Browne, P. Doornenbal, J. Lee, A. Obertelli, Y. Tsunoda, T. Otsuka, Y. Chazono, G. Hagen, J. D. Holt, G. R. Jansen, K. Ogata, N. Shimizu, Y. Utsuno, K. Yoshida, N. L. Achouri, H. Baba, D. Calvet, F. Château, N. Chiga *et al.*, Phys. Lett. B **843**, 138205 (2023).

[13] H. Scheit, T. Glasmacher, B. A. Brown, J. A. Brown, P. D. Cottle, P. G. Hansen, R. Harkewicz, M. Hellström, R. W. Ibbotson, J. K. Jewell, K. W. Kemper, D. J. Morrissey, M. Steiner, P. Thirolf, and M. Thoennessen, Phys. Rev. Lett. **77**, 3967 (1996).

[14] S. Calinescu, L. Cáceres, S. Grévy, O. Sorlin, Z. Dombrádi, M. Stanoiu, R. Astabatyan, C. Borcea, R. Borcea, M. Bowry, W. Catford, E. Clément, S. Franchoo, R. Garcia, R. Gillibert, I. H. Guerin, I. Kuti, S. Lukyanov, A. Lepailleur, V. Maslov *et al.*, Phys. Rev. C **93**, 044333 (2016).

[15] R. F. Garcia Ruiz, M. L. Bissell, K. Blaum, A. Ekström, N. Frömmgen, G. Hagen, M. Hammen, K. Hebeler, J. D. Holt, G. R. Jansen, M. Kowalska, K. Kreim, W. Nazarewicz, R. Neugart, G. Neyens, W. Nörtershäuser, T. Papenbrock, J. Papuga, A. Schwenk, J. Simonis *et al.*, Nat. Phys. **12**, 594 (2016).

[16] M. Enciu, H. N. Liu, A. Obertelli, P. Doornenbal, F. Nowacki, K. Ogata, A. Poves, K. Yoshida, N. L. Achouri, H. Baba, F. Browne, D. Calvet, F. Château, S. Chen, N. Chiga, A. Corsi, M. L. Cortés, A. Delbart, J.-M. Gheller, A. Giganon *et al.*, Phys. Rev. Lett. **129**, 262501 (2022).

[17] J. Bonnard, S. M. Lenzi, and A. P. Zuker, Phys. Rev. Lett. **116**, 212501 (2016).

[18] M. Williams-Norton and R. Abegg, Nucl. Phys. A **291**, 429 (1977).

[19] J. Hanspal, N. Clarke, R. Griffiths, O. Karban, and S. Roman, Nucl. Phys. A **436**, 236 (1985).

[20] D.-C. Dinca, R. V. F. Janssens, A. Gade, D. Bazin, R. Broda, B. A. Brown, C. M. Campbell, M. P. Carpenter, P. Chowdhury, J. M. Cook, A. N. Deacon, B. Fornal, S. J. Freeman, T. Glasmacher, M. Honma, F. G. Kondev, J.-L. Lecouey, S. N. Liddick, P. F. Mantica, W. F. Mueller *et al.*, Phys. Rev. C **71**, 041302(R) (2005).

[21] A. Goldkuhle, C. Fransen, A. Blazhev, M. Beckers, B. Birkenbach, T. Braunroth, E. Clément, A. Dewald, J. Dudouet, J. Eberth, H. Hess, B. Jacquot, J. Jolie, Y.-H. Kim, A. Lemasson,

S. M. Lenzi, H. J. Li, J. Litzinger, C. Michelagnoli, C. Müller-Gatermann *et al.* (AGATA Collaboration), Phys. Rev. C **100**, 054317 (2019).
[22] J. Prisciandaro, P. Mantica, B. Brown, D. Anthony, M. Cooper, A. Garcia, D. Groh, A. Komives, W. Kumarasiri, P. Lofy, A. Oros-Peusquens, S. Tabor, and M. Wiedeking, Phys. Lett. B **510**, 17 (2001).
[23] Z. Meisel, S. George, S. Ahn, J. Browne, D. Bazin, B. A. Brown, J. F. Carpino, H. Chung, R. H. Cyburt, A. Estradé, M. Famiano, A. Gade, C. Langer, M. Matoš, W. Mittig, F. Montes, D. J. Morrissey, J. Pereira, H. Schatz, J. Schatz *et al.*, Phys. Rev. Lett. **114**, 022501 (2015).
[24] M. Mougeot, D. Atanasov, C. Barbieri, K. Blaum, M. Breitenfeld, A. de Roubin, T. Duguet, S. George, F. Herfurth, A. Herlert, J. D. Holt, J. Karthein, D. Lunney, V. Manea, P. Navrátil, D. Neidherr, M. Rosenbusch, L. Schweikhard, A. Schwenk, V. Somà *et al.*, Phys. Rev. C **102**, 014301 (2020).
[25] A. Gade, D. Bazin, C. M. Campbell, J. A. Church, D. C. Dinca, J. Enders, T. Glasmacher, Z. Hu, K. W. Kemper, W. F. Mueller, H. Olliver, B. C. Perry, L. A. Riley, B. T. Roeder, B. M. Sherrill, and J. R. Terry, Phys. Rev. C **68**, 014302 (2003).
[26] R. Winkler, A. Gade, T. Baugher, D. Bazin, B. A. Brown, T. Glasmacher, G. F. Grinyer, R. Meharchand, S. McDaniel, A. Ratkiewicz, and D. Weisshaar, Phys. Rev. Lett. **108**, 182501 (2012).
[27] H. N. Liu, A. Obertelli, P. Doornenbal, C. A. Bertulani, G. Hagen, J. D. Holt, G. R. Jansen, T. D. Morris, A. Schwenk, R. Stroberg, N. Achouri, H. Baba, F. Browne, D. Calvet, F. Château, S. Chen, N. Chiga, A. Corsi, M. L. Cortés, A. Delbart *et al.*, Phys. Rev. Lett. **122**, 072502 (2019).
[28] D. Steppenbeck, S. Takeuchi, N. Aoi, P. Doornenbal, M. Matsushita, H. Wang, Y. Utsuno, H. Baba, S. Go, J. Lee, K. Matsui, S. Michimasa, T. Motobayashi, D. Nishimura, T. Otsuka, H. Sakurai, Y. Shiga, N. Shimizu, P.-A. Söderström, T. Sumikama *et al.*, Phys. Rev. Lett. **114**, 252501 (2015).
[29] M. L. Cortés, P. Doornenbal, M. Dupuis, S. M. Lenzi, F. Nowacki, A. Obertelli, S. Péru, N. Pietralla, V. Werner, K. Wimmer, G. Authelet, H. Baba, D. Calvet, F. Château, A. Corsi, A. Delbart, J.-M. Gheller, A. Gillibert, T. Isobe, V. Lapoux *et al.*, Phys. Rev. C **97**, 044315 (2018).
[30] L. Gaudefroy, O. Sorlin, D. Beaumel, Y. Blumenfeld, Z. Dombrádi, S. Fortier, S. Franchoo, M. Gélin, J. Gibelin, S. Grévy, F. Hammache, F. Ibrahim, K. Kemper, K. L. Kratz, S. M. Lukyanov, C. Monrozeau, L. Nalpas, F. Nowacki, A. N. Ostrowski, Y. E. Penionzhkevich *et al.*, Eur. Phys. J. A **27**, 309 (2006).
[31] S. Péru, M. Girod, and J. F. Berger, Eur. Phys. J. A **9**, 35 (2000).
[32] R. Rodríguez-Guzmán, J. L. Egido, and L. M. Robledo, Phys. Rev. C **65**, 024304 (2002).
[33] S. Hilaire and M. Girod, Eur. Phys. J. A **33**, 237 (2007).
[34] http://www-phynu.cea.fr.
[35] J. P. Delaroche, M. Girod, J. Libert, H. Goutte, S. Hilaire, S. Péru, N. Pillet, and G. F. Bertsch, Phys. Rev. C **81**, 014303 (2010).
[36] B. D. Linh, A. Corsi, A. Gillibert, A. Obertelli, P. Doornenbal, C. Barbieri, S. Chen, L. X. Chung, T. Duguet, M. Gómez-Ramos, J. D. Holt, A. Moro, P. Navrátil, K. Ogata, N. T. T. Phuc, N. Shimizu, V. Somà, Y. Utsuno, N. L. Achouri, H. Baba *et al.*, Phys. Rev. C **104**, 044331 (2021).
[37] T. Kubo, D. Kameda, H. Suzuki, N. Fukuda, H. Takeda, Y. Yanagisawa, M. Ohtake, K. Kusaka, K. Yoshida, N. Inabe, T. Ohnishi, A. Yoshida, K. Tanaka, and Y. Mizoi, Prog. Theor. Exp. Phys **2012**, 03C003 (2012).
[38] N. Fukuda, T. Kubo, T. Ohnishi, N. Inabe, H. Takeda, D. Kameda, and H. Suzuki, Nucl. Instrum. Methods Phys. Res. B **317**, 323 (2013).
[39] A. Obertelli, A. Delbart, S. Anvar, L. Audirac, G. Authelet, H. Baba, B. Bruyneel, D. Calvet, F. Château, A. Corsi, P. Doornenbal, J.-M. Gheller, A. Giganon, C. Lahonde-Hamdoun, D. Leboeuf, D. Loiseau, A. Mohamed, J.-Ph. Mols, H. Otsu, C. Péron, Eur. Phys. J. A **50**, 8 (2014).
[40] T. Kobayashi, N. Chiga, T. Isobe, Y. Kondo, T. Kubo, K. Kusaka, T. Motobayashi, T. Nakamura, J. Ohnishi, H. Okuno, H. Otsu, T. Sako, H. Sato, Y. Shimizu, K. Sekiguchi, K. Takahashi, R. Tanaka, and K. Yoneda, Nucl. Instrum. Methods Phys. Res. B **317**, 294 (2013).
[41] S. Takeuchi, T. Motobayashi, Y. Togano, M. Matsushita, N. Aoi, K. Demichi, H. Hasegawa, and H. Murakami, Nucl. Instrum. Methods Phys. Res., Sect. A **763**, 596 (2014).
[42] M. Wang, W. Huang, F. Kondev, G. Audi, and S. Naimi, Chin. Phys. C **45**, 030003 (2021).
[43] K. Boretzky, I. Gaăparić, M. Heil, J. Mayer, A. Heinz, C. Caesar, D. Kresan, H. Simon, H. Törnqvist, D. Körper, G. Alkhazov, L. Atar, T. Aumann, D. Bemmerer, S. Bondarev, L. Bott, S. Chakraborty, M. Cherciu, L. Chulkov, M. Ciobanu *et al.*, Nucl. Instrum. Methods Phys. Res., Sect. A **1014**, 165701 (2021).
[44] T. Nakamura and Y. Kondo, Nucl. Instrum. Methods Phys. Res. B **376**, 156 (2016).
[45] S. Chen, J. Lee, P. Doornenbal, A. Obertelli, C. Barbieri, Y. Chazono, P. Navrátil, K. Ogata, T. Otsuka, F. Raimondi, V. Somà, Y. Utsuno, K. Yoshida, H. Baba, F. Browne, D. Calvet, F. Château, N. Chiga, A. Corsi, M. L. Cortés *et al.*, Phys. Rev. Lett. **123**, 142501 (2019).
[46] Y. Sun, A. Obertelli, P. Doornenbal, C. Barbieri, Y. Chazono, T. Duguet, H. Liu, P. Navrátil, F. Nowacki, K. Ogata, T. Otsuka, F. Raimondi, V. Somà, Y. Utsuno, K. Yoshida, N. Achouri, H. Baba, F. Browne, D. Calvet, F. Château *et al.*, Phys. Lett. B **802**, 135215 (2020).
[47] A. M. Moro, Phys. Rev. C **92**, 044605 (2015).
[48] T. Wakasa, K. Ogata, and T. Noro, Prog. in Part. and Nucl. Phys. **96**, 32 (2017).
[49] T. Aumann, C. A. Bertulani, and J. Ryckebusch, Phys. Rev. C **88**, 064610 (2013).
[50] K. Ogata, K. Yoshida, and K. Minomo, Phys. Rev. C **92**, 034616 (2015).
[51] R. E. Kass and A. E. Raftery, J. Am. Stat. Assoc. **90**, 773 (1995).
[52] I. Murray, F. Browne, S. Chen, M. L. Cortés, P. Doornenbal, H. Sakurai, J. Lee, M. MacCormick, W. Rodriguez, V. Vaquero, D. Steppenbeck, and K. Wimmer, RIKEN Accel. Prog. Rep. **51**, 148 (2018).
[53] T. Aumann, C. Barbieri, D. Bazin, C. Bertulani, A. Bonaccorso, W. Dickhoff, A. Gade, M. Gómez-Ramos, B. Kay, A. Moro, T. Nakamura, A. Obertelli, K. Ogata, S. Paschalis, and T. Uesaka, Prog. Part. Nucl. Phys. **118**, 103847 (2021).
[54] M. Gómez-Ramos and A. Moro, Phys. Lett. B **785**, 511 (2018).
[55] S. Goriely, S. Hilaire, M. Girod, and S. Péru, Phys. Rev. Lett. **102**, 242501 (2009).
[56] J. Dechargé and D. Gogny, Phys. Rev. C **21**, 1568 (1980).
[57] Y. Utsuno, T. Otsuka, B. A. Brown, M. Honma, T. Mizusaki, and N. Shimizu, Phys. Rev. C **86**, 051301(R) (2012).

[58] S. Péru and M. Martini, Eur. Phys. J. A **50**, 88 (2014).
[59] S. Goriely, S. Péru, G. Colò, X. Roca-Maza, I. Gheorghe, D. Filipescu, and H. Utsunomiya, Phys. Rev. C **102**, 064309 (2020).
[60] S. R. Stroberg, H. Hergert, S. K. Bogner, and J. D. Holt, Annu. Rev. Nucl. Part. Sci. **69**, 307 (2019).
[61] V. Somà, T. Duguet, and C. Barbieri, Phys. Rev. C **84**, 064317 (2011).
[62] V. Somà, Front. Phys. **8**, 340 (2020).
[63] S. R. Stroberg, A. Calci, H. Hergert, J. D. Holt, S. K. Bogner, R. Roth, and A. Schwenk, Phys. Rev. Lett. **118**, 032502 (2017).
[64] T. Miyagi, S. R. Stroberg, P. Navrátil, K. Hebeler, and J. D. Holt, Phys. Rev. C **105**, 014302 (2022).
[65] S. R. Stroberg (private communication).
[66] K. Hebeler, S. K. Bogner, R. J. Furnstahl, A. Nogga, and A. Schwenk, Phys. Rev. C **83**, 031301(R) (2011).
[67] W. G. Jiang, A. Ekström, C. Forssén, G. Hagen, G. R. Jansen, and T. Papenbrock, Phys. Rev. C **102**, 054301 (2020).
[68] V. Somà, P. Navrátil, F. Raimondi, C. Barbieri, and T. Duguet, Phys. Rev. C **101**, 014318 (2020).
[69] A. Ekström, G. R. Jansen, K. A. Wendt, G. Hagen, T. Papenbrock, B. D. Carlsson, C. Forssén, M. Hjorth-Jensen, P. Navrátil, and W. Nazarewicz, Phys. Rev. C **91**, 051301(R) (2015).
[70] S. R. Stroberg, imsrg + +, https://github.com/ragnarstroberg/imsrg.
[71] N. Shimizu, T. Mizusaki, Y. Utsuno, and Y. Tsunoda, Comput. Phys. Commun. **244**, 372 (2019).